Solid Earth, 8, 751–765, 2017
https://doi.org/10.5194/se-8-751-2017

Solid Earth Open Access EGU

Microscale and nanoscale strain mapping techniques applied to creep of rocks

Alejandra Quintanilla-Terminel[1], Mark E. Zimmerman[1], Brian Evans[2], and David L. Kohlstedt[1]

[1]Department of Earth Sciences, University of Minnesota, Minneapolis, MN 55455, USA
[2]Earth, Atmospheric and Planetary Sciences, Massachusetts Institute of Technology, Cambridge, MA 02139, USA

Correspondence to: Alejandra Quintanilla-Terminel (aqt@alum.mit.edu)

Received: 8 March 2017 – Discussion started: 15 March 2017
Revised: 26 May 2017 – Accepted: 8 June 2017 – Published: 10 July 2017

Abstract. Usually several deformation mechanisms interact to accommodate plastic deformation. Quantifying the contribution of each to the total strain is necessary to bridge the gaps from observations of microstructures, to geomechanical descriptions, to extrapolating from laboratory data to field observations. Here, we describe the experimental and computational techniques involved in microscale strain mapping (MSSM), which allows strain produced during high-pressure, high-temperature deformation experiments to be tracked with high resolution. MSSM relies on the analysis of the relative displacement of initially regularly spaced markers after deformation. We present two lithography techniques used to pattern rock substrates at different scales: photolithography and electron-beam lithography. Further, we discuss the challenges of applying the MSSM technique to samples used in high-temperature and high-pressure experiments. We applied the MSSM technique to a study of strain partitioning during creep of Carrara marble and grain boundary sliding in San Carlos olivine, synthetic forsterite, and Solnhofen limestone at a confining pressure, P_c, of 300 MPa and homologous temperatures, T/T_m, of 0.3 to 0.6. The MSSM technique works very well up to temperatures of 700 °C. The experimental developments described here show promising results for higher-temperature applications.

1 Introduction

During plastic deformation of a crystalline material, strain is accommodated by a variety of deformation mechanisms, including atomic diffusion, mechanical twinning, grain boundary sliding, and dislocation glide, climb, and cross slip, which may operate separately or in combination. Deformation mechanism maps are conceptual tools that divide stress, temperature, and strain rate space into different fields with a particular deformation mechanism prevalent in each. Simplified flow laws are established by assuming specific micromechanical models corresponding to the prevalent mechanisms and using experimental data to fit the material constants in the theoretical flow laws (Ashby, 1972; Frost and Ashby, 1982). Such simplified flow laws are a useful first step for the extrapolation of laboratory results to larger-scale geomechanical problems, but it is also possible that the relative activity of the various deformation processes might change significantly when extended to natural conditions of rate, mean pressure, chemical environment, and temperature. Thus, the quantification of the strain due to each process and the determination of the interactions among the processes is crucial for establishing robust microphysical models that can be used to interpret observations of natural microstructures and nanostructures and that can describe natural deformation at larger spatial and temporal scales.

Quantification of the strain accommodated by each mechanism is not an easy task. Ideally, the microstructural evolution of a polycrystalline material would be monitored continuously as a sample is strained. However, high pressures and temperatures are required when deforming rocks through plastic or viscous processes in the laboratory, making microscopic observations of deformation in situ a significant experimental challenge. Fortunately, even stepwise observations of the amount of strain accommodated by individual intracrystalline mechanisms could significantly enhance our understanding of high-temperature creep.

In this paper, we describe a technique for microscale strain measurement (MSSM), which permits strain mapping at micrometer and submicrometer scales, and discuss several observations of strain partitioning in rocks deformed at high pressures and temperatures. To quantify the deformation, the coordinates of the material points (at the microscale) must be identified before and after deformation. Then, the strain tensor can be computed from their relative displacements. We used two lithography techniques, described in Sect. 2, to print a grid of points onto the polished surface of a rock. After deformation, we computed strain following the formulation described in Sect. 3. We applied the MSSM technique to four different high-temperature experiments described in Sect. 4.

2 Lithographic techniques

The literal meaning of lithography, writing on stones, is very appropriate for our application. More generally, lithography refers to different printing techniques that allow a pattern to be transferred onto a substrate. Microlithograpy and nanolithography are widely used in the semiconductor industry (Razegui, 2006; Mack, 2006) to pattern micrometric and nanometric circuits onto silicon wafers. Applying these techniques to nonconductive, heterogeneous materials is challenging, but we developed two protocols using photolithography and electron-beam (e-beam) lithography to produce patterns on the surfaces of Carrara marble, Solnhofen limestone, San Carlos olivine, and synthetic forsterite. The patterns had features with spatial dimensions on the order of 1 µm down to tens of nanometers. In this section, we will first describe both lithographic processes and then provide the specific protocols used for our applications. The communities developing and using microfabrication and nanofabrication techniques are extremely active. Undoubtedly, new processes and improvements will allow for other innovative applications to geomaterials.

2.1 Photolithography and e-beam lithography

Figure 1 summarizes the steps needed for the lithographic process. Both photolithography and electron-beam lithography require special equipment, which is usually present in standard clean laboratories used to fabricate solid-state devices. The process described here is commonly referred as "lift-off" in the microfabrication community. It uses a sacrificial layer of polymer, which is a film that can be spread uniformly on the sample, to create a pattern on the sample surface (Razeghi, 2006). Note that the microfabrication processes used in solid-state engineering require extra steps to ensure the functionalities of the devices (conductivity and reflectivity, among others). We present the steps required to deposit micrometric and nanometric patterns on a rock surface with the main objective of printing a particular

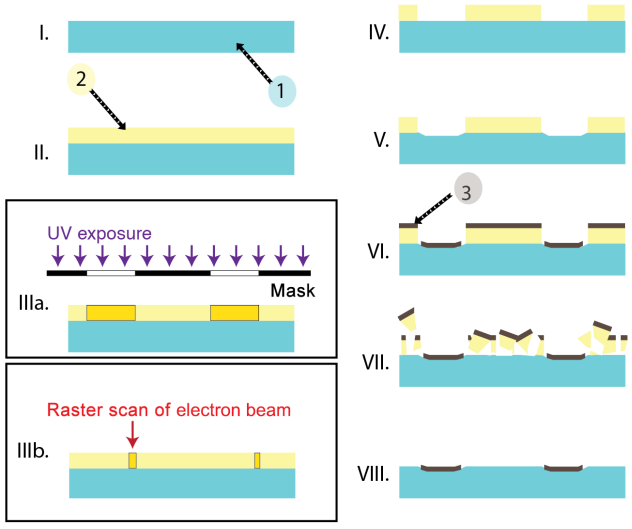

Figure 1. Lithographic process: (1) rock, (2) photoresist or PMMA, and (3) metal layer (sputtered or evaporated). Each step is described in more detail in the text: (I) sample preparation, (II) coating with a polymer (photoresist for photolithography, PMMA for e-beam lithography), (III) exposure to UV rays for photolithography (IIIa) or an electron beam for e-beam lithography (IIIb), (IV) development of the coating, (V) etching, (VI) metal deposition, (VII) dissolution of the remaining polymer, and (VIII) patterned sample.

grid designed to track strain at a granular level. Quintanilla-Terminel (2014) describes in more detail the different exploratory steps that were taken before developing the following protocols.

I. Sample preparation: the surface to be patterned needs to be polished to a roughness of less than 0.5 µm. The details of the polishing technique will depend on the composition, porosity, and grain size of the rock. For e-beam lithography, the sample must be flat with less than 1 µm of variation in height for each 1 mm^2 region.

II. Coating with a polymer: the surface then needs to be uniformly coated with a polymer sensitive to the energy used to transfer the pattern. A photoresist is sensitive to UV light (photolithography) and poly(methyl methacrylate), or PMMA, is sensitive to an electron beam (e-beam lithography). The coating method will depend on the sample geometry. Spin coating is the standard method for flat samples. The sample is held on a rotating device by a vacuum chuck and the polymer is spread onto the surface to uniform thickness by spinning the sample at a controlled speed, typically around 3000 rpm. For more challenging geometries, such as half cylinders or curved surfaces, a paintbrush or an aerosol spray can be used, but care must be taken to ensure that the polymer thickness is relatively uniform from sample to sample.

III. Exposure to UV rays for photolithography (IIIa) or an electron beam for e-beam lithography (IIIb). Although both techniques allow for the transfer of a custom-designed pattern, the process by which this is achieved is different. Photolithography necessitates the creation of a shadow mask, which is a glass mask imprinted with the wanted design analogous to a negative in the photographic process. UV light is then shined through the mask onto the sample coated with the photoresist. E-beam lithography does not necessitate a mask; instead the pattern is directly rastered with an electron beam at a specific dose (typically set at around 500 to 1000 $\mu C\,cm^{-2}$) onto the PMMA covering the sample. The correct exposure time and the dose of the electron beam depend on the nature of the polymer used, its thickness, the chemistry of the substrate, and the resolution of the pattern. For both photolithography and e-beam lithography, the pattern can be overexposed or underexposed. Overexposed features or patterns will appear larger than designed, while those underexposed will be smaller or will not appear at all.

IV. Development of the coating: the structure of the polymer exposed to the UV light or to the electron beam changes, and a chemical bath is used to dissolve this sacrificial layer. The pattern is now exposed on the sample surface. The development time depends on the exposure time and on the resolution of the pattern. Some play exists between the exposure time and the development time; ultimately, the lithographer must determine the optimum match for the intended application.

V. Etching: the exposed surface is slightly etched before proceeding to the metal deposition. This step was found to be important in geomaterials to allow for a good adhesion of the metal layer. The etching step can be dry (via reactive or nonreactive gas) or wet (typically in a diluted HCl or HF bath). If the sample cannot be in contact with water, a dry etch would be preferable.

VI. Metal deposition: a physical vapor deposition is used to coat the sample surface with a thin film of a chosen metal. There is latitude in the choice of the metal sputtered. Our applications require a metal that can be seen before and after deformation and that has a minimum interaction with the rock. Therefore, the parameters that are important in the choice of metal include adhesion, melting temperature, visibility, and interactions with the rock.

VII. Dissolution of the remaining polymer: the remaining polymer is dissolved, leaving only the metal deposited onto the sample surface.

VIII. Patterned sample: the patterned sample is now ready to be deformed.

Both photolithography and e-beam lithography can be used for decorating rocks; a combination of both would also be possible. The main factors to take into account are the size of the area on which the pattern will be deposited, the design of the pattern (shape and resolution), and the sample geometry. Photolithography is a good choice when many samples are required, when large areas are to be patterned, and when the sample geometry is more complicated. For applications requiring a pattern with submicron features, e-beam lithography will be more appropriate. Because e-beam lithography does not necessitate a mask, it would be faster to implement for single applications. In the following sections we provide a detailed protocol for each technique. With some adaptation, particularly regarding the exposure, developing steps, and the choice of the metal to be deposited, these protocols might be used on other geomaterials.

2.2 Photolithography applied to Carrara marble

Photolithography was carried out at the MIT Microsystems Technology Laboratory (MTL), where half cylinders of Carrara marble were patterned. First, each half cylinder was polished with a succession of aluminum oxide suspensions down to a 0.5 µm particle size to produce a flat, mirror-like surface. After polishing, the pattern was produced using the following steps.

I. The polished half cylinders were dried in a convection oven at 130 °C for 20 min.

II. The sample surfaces were manually coated with a light-sensitive photoresist, Fujifilm OCG 825 g-line, using a paintbrush; the thickness of the polymer was determined to be $\sim$ 400 nm using a profilometer. Each half cylinder was then baked for 20 min in a convection oven at 90 °C.

III. The pattern inscribed in a photomask was transferred onto the polymer coating by exposing the coating to ultraviolet light in a mask aligner for 60 s. The exposure time depends on the substrate, the photoresist, and photoresist thickness. Our photomask was created using computer-aided design (CAD) software to create the pattern and a laser to draw the pattern onto a glass plate covered with chrome and photoresist, followed by a typical etch-back technique (Mack, 2006). Photomasks are also available from various commercial sources in the microfabrication industry.

IV. The nonexposed polymer was dissolved using a developer, Fujifilm OCG 934, for 30 to 60 s.

V. The samples were then very lightly etched with an acidic solution (a 1 mass % dilute solution of HCl for 1 s).

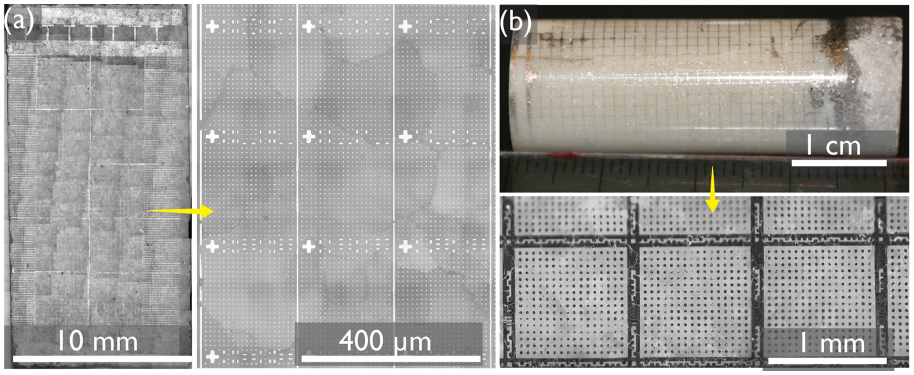

Figure 2. Patterned Carrara marble using photolithography. **(a)** The optical light micrograph on the left shows the patterned half cylinder with more than 1.5 million markers, while the micrograph on the right presents a zoomed-in view of an area revealing the 2 µm wide markers with centers spaced every 10 µm and the embedded numbering system that allows us to locate each marker before and after deformation. **(b)** The photograph on top illustrates the structure of a patterned cylinder, while the optical light micrograph on the bottom shows a closer view of the patterned curved surface revealing 20 µm wide markers with centers spaced every 50 µm.

VI. The surface of the samples was sputtered with a double layer composed of 20 nm of chromium and 30 nm of gold using a plasma sputterer.

VII. Finally, the protective layer of photoresist was removed with 2-(2-aminoethoxy)ethanol, N-methyl-2-pyrrolidine at 100 °C for 30 min.

Photolithography is a very flexible patterning technique. Patterns can be deposited on large surfaces with a customized design, little limitation exists regarding the geometry of the sample, and a wide selection of metals can be used. For example, the 10×20 mm patterned area in Fig. 2a contains roughly 1.5 million markers spaced every 10 µm and is composed of a double layer of chromium and gold. The polished surface of the outside of a Carrara marble cylinder in Fig. 2b is patterned with markers spaced every 50 µm and composed of a double layer of titanium and gold. The main disadvantages of photolithography are related to pattern resolution. Although the resolution of photolithography has been pushed to submicrometric scales (Dong et al., 2014), the resolution is limited to a few micrometers for nonconventional substrates like rocks and to hundreds of micrometers for patterns on curved surfaces. Furthermore, a photomask is needed, and its fabrication adds an additional step to the protocol. More details on the photolithography process and the development of the described protocol are given by Quintanilla-Terminel (2014) and Quintanilla-Terminel and Evans (2016).

2.3 Electron-beam lithography applied to olivine and Solnhofen limestone

The e-beam lithography process was carried out at the Minnesota Nano Center (MNC). The forsterite and San Carlos olivine samples were polished using diamond-lapping film down to a 0.5 µm particle size. The Solnhofen limestone samples were polished with aluminum oxide powder following the same procedure used on the Carrara marble samples. The electron-beam lithography steps are described below.

I. A wafer of San Carlos olivine, Solnhofen limestone, or synthetic forsterite was initially left in a vacuum oven at 130 °C for 20 min to dry.

II. The sample was first coated with PMMA diluted in 4 vol % chlorobenzene. The coating was done with a precision spin coater spinning at 3000 rpm for 60 s to produce a thickness of the PMMA film of 350 nm (evaluated with ellipsometry). The sample was then baked on a hot plate at 180 °C for 10 min. Afterward, the sample was coated with 15 nm of gold in a plasma sputterer to avoid charging.

III. The patterning was achieved using a Vistec EBPG5000+ e-beam lithography system. First, the design was created using CAD software. In e-beam lithography, a dose array is typically used in order to find the optimum exposure dose for each material and each resolution. To find the optimum exposure for San Carlos olivine, forsterite, and Solnhofen limestone, patterns of different resolution were exposed with doses ranging from 300 to 1200 µC cm^{-2} in increments of 50 µC cm^{-2}. The optical microscope image in Fig. 3a illustrates the results of a dose array performed on a sample of San Carlos olivine. The visible radial lines forming the spokes of a wheel are 10 µm thick and were exposed to 900 µC cm^{-2}. Inside each rectangle along the radial lines, different doses were tested for grids lines of 50, 100, and 200 nm in width. Examples of good exposure and overexposure are shown in the secondary electron micrographs in Fig. 3a and b, respectively. Based on these results, we selected optimal doses of 900 µC cm^{-2} for submicron features, 750 µC cm^{-2} for micrometer features on San Carlos

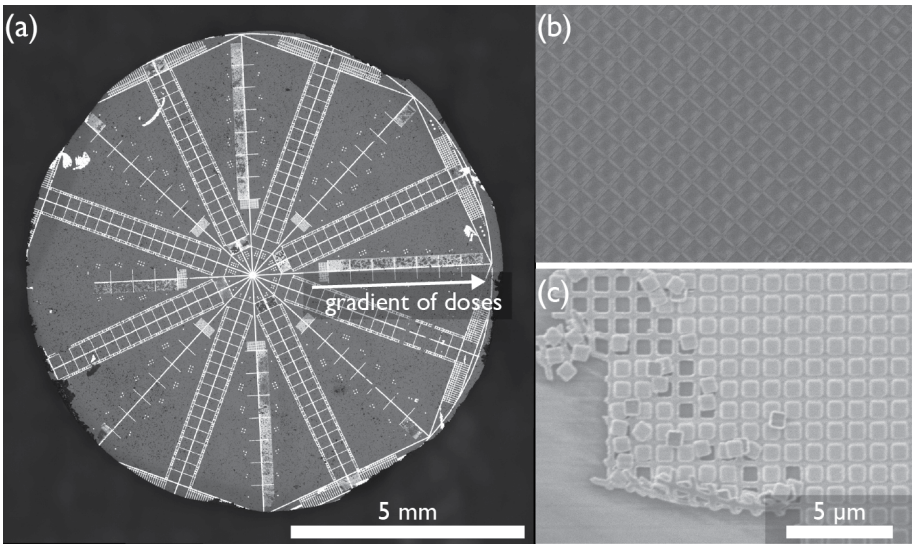

Figure 3. (a) Light micrograph of a patterned San Carlos olivine crystal. Electron-beam lithography was used with varying doses along the radial lines. All radial lines 10 µm thick and exposed to a 900 µC cm^{-2} dose are visible; inside each rectangle different doses were tested: examples of a well-exposed and an overexposed area are seen in panel **(b)** and **(c)**, respectively. In the overexposed area, the pattern appears blurred, and causes the rounding of the corners in the grid. An underexposed area will typically show no signs of the pattern. The dose test allowed for the identification of the optimum dose to achieve the desired resolution: 700 µC cm^{-2} for 200 nm wide lines.

olivine and synthetic forsterite, and 800 µC cm^{-2} for the submicron features on Solnhofen limestone. A variety of layouts were designed to meet the needs of the type of application; for example, the wheel design (Fig. 3a) was developed to evaluate the inelastic strain distribution produced during a torsion experiment.

IV. The first step in the developing process required the dissolution of the gold layer using a solution of KI, routinely called a gold etcher. The sample was first submerged in the KI solution for 30 s, then rinsed in deionized (DI) water for 10 s, and finally rinsed in isopropanol for 10 s. The sample was then developed. Two developing processes were explored. The typical developing solution for PMMA is a 3 : 1 mixture of isopropanol and methyl isobutyl ketone. The coated sample was submerged in this solution for 60 s. If a higher resolution is required during developing, a mixture of 3 : 1 isopropanol and DI water can be used. This second mixture was used with samples that were exposed to about half of the dose previously described in order to avoid overdeveloping the features (Yasin et al., 2002). In any case, the choice of the particular developer, exposure, and developing time should be adapted to the patterned substrate and the resolution needed.

V. Two etching processes were explored; a wet etch using HF diluted to 1 vol % applied for 1 s and a chlorine-gas etch using an Oxford plasma etcher for 1 min. Although the two processes produced similar results, the wet etch was simpler to implement.

VI. A 110 nm thick layer of Cr was deposited in a plasma evaporator.

VII. To dissolve the remaining PMMA, the sample was immersed in 2-(2-aminoethoxy)ethanol, N-methyl-2-pyrrolidine at 120 °C for at least 4 h. Gentle, 1 s bursts of sonication were sometimes necessary to completely remove the PMMA.

The resulting patterned surfaces of San Carlos olivine and Solnhofen limestone are illustrated in Fig. 4. Notice the difference in scale compared to the patterned marble surface in Fig. 2; the images of the patterned Carrara marble in Fig. 2 are optical light micrographs, whereas the images of the San Carlos and Solnhofen limestone in Fig. 4 are scanning secondary-electron micrographs. The high resolution, the sharpness of lines, and the pattern profile can be better appreciated in images of the patterns deposited on San Carlos olivine obtained by atomic-force microscopy (AFM; Fig. 5). It is apparent that electron-beam lithography permits much higher resolution than photolithography; in theory, nanometer scales can be achieved (Vieu et al., 2000; Manfrinato et al., 2013). For geomaterials, a resolution of 20 nm is easily attained. The pattern is rastered directly onto the sample without the need for a mask, which facilitates tests with different designs. However, because the rastering process has to be repeated for each sample, e-beam lithography is much slower and more costly than photolithography. Furthermore, samples have to fit into the electron-beam lithography system, limiting the geometry of the sample that can be patterned. In the Vistec EBPG5000+ used at the MNC at the

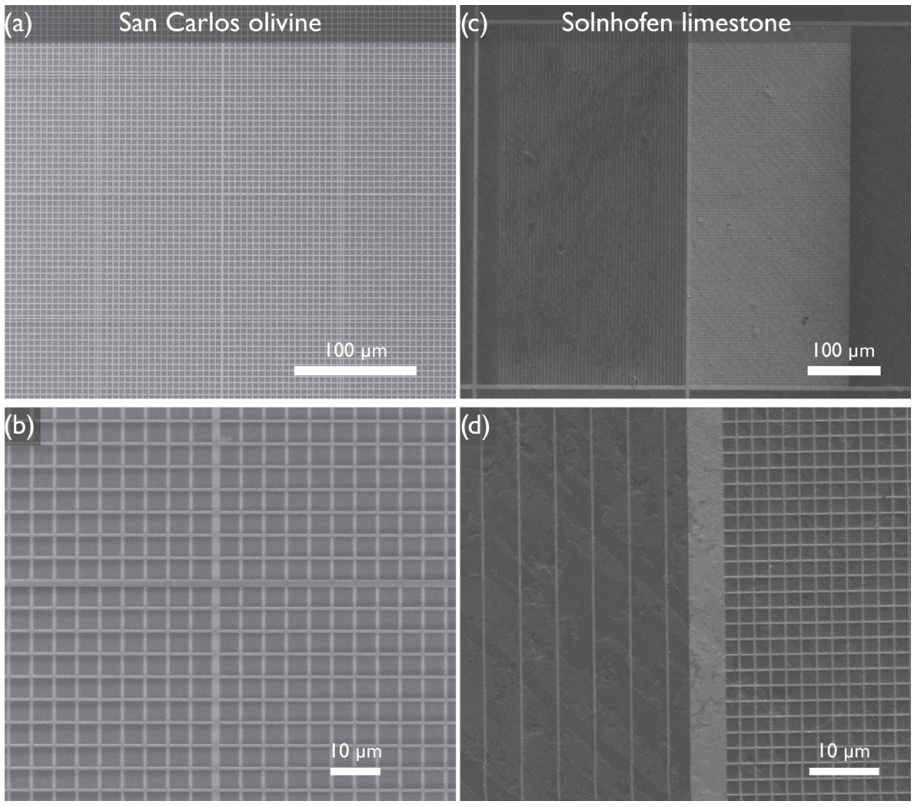

Figure 4. Secondary electron images of patterned San Carlos olivine **(a, b)** and Solnhofen limestone **(c, d)**. The grid in the San Carlos olivine sample is composed of 500 µm lines spaced every 4.5 µm **(a)**; a zoom in is seen in panel **(b)**. For Solnhofen limestone, we combined 200 nm straight lines with a regular grid of 200 µm lines spaced every 2 µm **(c)**; a zoom into both areas is seen in panel **(d)**.

University of Minnesota, the sample has to be as thin and flat as a silicon wafer (i.e., no more than 1 mm thick), which is a geometric constraint that has to be considered when designing deformation experiments.

3 Strain analysis

The regular grid that is printed onto the sample is used to track the strain accommodated by the sample. Indeed, the ultimate goal of using the MSSM technique is to understand which micromechanical processes accommodate strain in a deforming rock and to relate the observed microstructure to the imposed macroscopic deformation conditions. For this purpose, it is necessary to calculate the local strains using microscale gauge lengths within larger regions of interest.

3.1 Need for a regular grid

Different techniques allow for the computation of strain at a local scale; most are image-based particle tracking techniques and therefore use a Lagrangian description in which strain is calculated by following a material point before and after deformation (Reddy, 2013; Malvern, 1969). The more widely used strain analysis technique, digital image correlation (DIC), has been successfully applied in a variety of rock mechanics applications. For instance, DIC was used to map the localization of damage in a heterogeneous carbonate (Dautriat et al., 2011), to quantify the role of crystal slip and grain boundary sliding during creep of synthetic halite (Bourcier et al., 2013), and to better understand creep of ice (Chauve et al., 2015; Grennerat et al., 2012). DIC is an excellent tool for extracting displacement and strain measurements at a microscopic scale (Bruck et al., 1987; Sutton et al., 2009) by comparing digital micrographs of the sample at different stages of deformation. The strain is computed using various algorithms that allow the observer to track blocks of pixels and cross correlate them between deformation steps (Bornert et al., 2008). Each block of pixels therefore needs to be unique and recognizable between deformation steps.

High-temperature and high-pressure deformation often changes the reflectivity of the material to a point at which blocks of pixels are no longer recognizable between deformation steps. Because our experimental setup makes it difficult to analyze incrementally strained samples, we require a technique that allows us to identify a material point independently of the amount of deformation the material has experienced. We therefore rely on the analysis of an initially regular grid characterized after deformation (Allais et al., 1994;

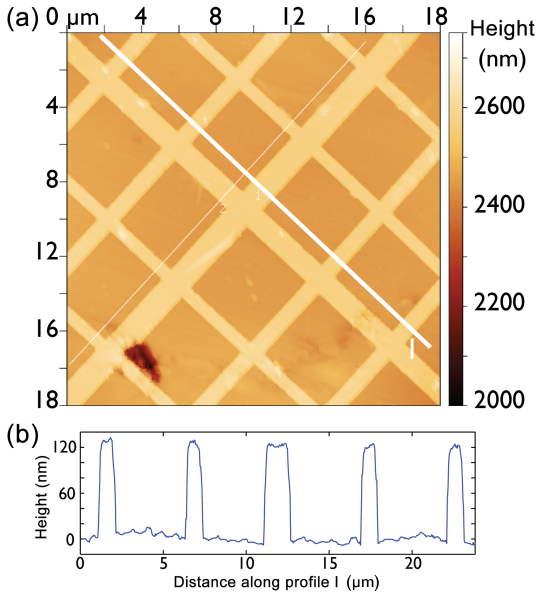

Figure 5. Atomic force micrographs of patterned San Carlos olivine **(a)** and the height profile **(b)** of the surface along profile 1. The 500 nm wide chromium lines are spaced every 4.5 µm and are 110 nm high. The sharpness of the lines can be appreciated in the AFM data.

Ghadbeigi et al., 2012; Karimi, 1984; Moulart et al., 2007; Sharpe, 2008; Wu et al., 2006; Martin et al., 2014). Because our experiments are performed at high temperature and high pressure with a metal jacket surrounding the sample, the grid is introduced in the middle of the sample, following different variations of a split-cylinder assembly (Raleigh, 1965). The initial reference grid is formed by deposition using either photolithography or e-beam lithography. Other deposition methods have been used, such as sputtering through a commercial screen (Xu and Evans, 2010) or introducing a metal mesh between the sample halves (Spiers, 1979). Recently, Hiraga (2015) used a focused ion beam to groove lines on samples composed of synthetic forsterite and diopside in order to track grain displacement and rotation during diffusion creep. In all the techniques, the main challenge is to accurately identify each individual marker or line before and after deformation. Various complications can arise; for instance, the markers can be unstable at high temperature, or the split-cylinder surfaces can weld together at high pressures, making the recovery of the patterned surface challenging or impossible. Nevertheless, if the identification of individual markers after deformation is accomplished, then spatial variations in relative displacement can be used to compute the strain field across the reference surface. Lithography has the advantages that higher resolutions can be achieved, the patterns are more robust and they survive high-temperature, high-pressure deformation, and the specific patterns can be custom designed to account for the grain size of the material or the research questions to be answered. Furthermore, because lithographic techniques allow the researcher to create extremely regular patterns with known dimensions, the strain can be computed by locating the markers only after deformation. It is, however, advisable to image the sample before deformation as well, as this step could provide additional information (particularly if the grain boundaries are visible) and eliminate the potential error introduced by irregularities in the undeformed grid.

3.2 Strain computation

3.2.1 Marker location

Different image processing techniques can be used for locating the markers before and after deformation, such as a convolution (Biery et al., 2003) or a Hough transform algorithm (Quintanilla-Terminel and Evans, 2016). Depending on the application, the user could rely on the regularity of the grid and not identify the markers before deformation. Often, some manual input is required to ensure that the marker is correctly identified after deformation.

3.2.2 The *n*-point analysis

The n-point analysis is an inversion technique that allows the user to probe the strain at different scales. The positions of n material points are registered before and after deformation, and the best fit of the deformation gradient tensor transforming the undeformed to the deformed material lines related to these n material points is computed. This inversion assumes that the deformation is homogenous over the area spanned by the n-point ensemble. In practice, the technique requires the following steps. (1) Imaging the region of interest (ROI) before deformation. Based on the size and spacing of the markers, this step can be performed with light or electron-beam microscopy. Note that the strain can also be computed without imaging the area before deformation, relying on the regularity of the grid. (2) Registration of the coordinates of all markers in the ROI before deformation. (3) Deformation experiments under pressure and temperature. (4) Imaging of the same ROI after deformation. (4) Registration of the coordinates of all markers in the ROI after deformation. (5) Determination of deformation gradient tensor $\mathbf{F}$ using the n-point inversion technique. To eliminate rigid-body translations, the material displacements are calculated relative to a moving centroid for every set of n points. That is, the coordinates of each point i before and after deformation, X_i and x_i, respectively, are referenced to the centroid of the set of n points before and after deformation, C_n and c_n. The 2-D deformation gradient tensor $\mathbf{F}$ is determined from the relation between material displacement vectors before, $\mathrm{d}\boldsymbol{X}_i = X_i - C_n$, and after deformation, $\mathrm{d}\boldsymbol{x}_i = x_i - c_n$ using a least-squares estimate.

The deformation gradient tensor, $\mathbf{F}$, is determined by calculating the least-squares fit for the ensemble of n material vectors, i.e., minimizing the sum of the squares of the differ-

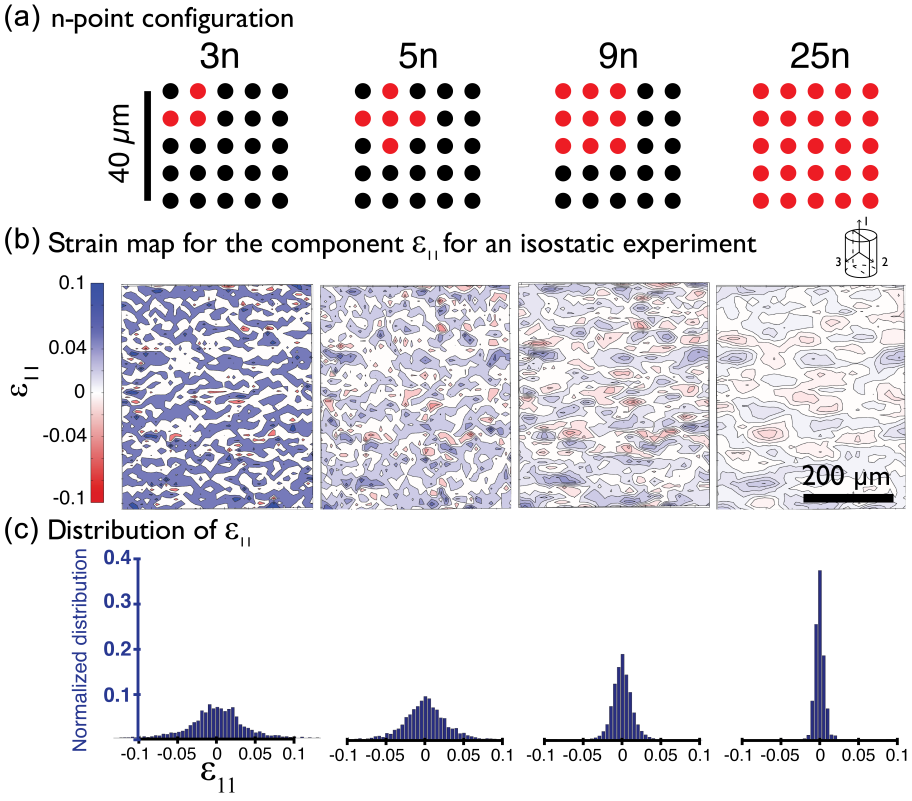

Figure 6. **(a)** The n-point configurations for $n = 3$, 5, 9, and 25. **(b)** Corresponding strain maps and strain distributions for strain along axis 1 in the sample reference (see insert for reference frame) for a Carrara marble cylinder isostatically annealed at $T = 700\,^{\circ}\mathrm{C}$ and $P_c = 300\,\mathrm{MPa}$ for 3 h. **(c)** Corresponding strain distribution for each strain map; it can be observed that the mean is always 0 but the spread of the distribution becomes smaller with increasing n. Modified after Quintanilla-Terminel and Evans (2016).

ence between the modeled and the measured material lines, $\mathrm{d}\boldsymbol{x}_i^* = \mathbf{F} \cdot \mathrm{d}\boldsymbol{X}$ and $\mathrm{d}\boldsymbol{x}_i$, respectively. Consequently, the tensor $\mathbf{F}$ describes the homogeneous deformation that best fits the displacement field of n material points. Four different configurations of n points are illustrated in Fig. 6a.

3.2.3 Computation of the strain tensor

The deformation gradient tensor $\mathbf{F}$ can be decomposed into a product of a rotation tensor $\mathbf{R}$ and either $\mathbf{U}$, a right-stretch tensor, or $\mathbf{V}$, a left-stretch tensor. $\mathbf{U}$ can be diagonalized following Eq. (1):

$$\mathbf{U} = \mathbf{Q}^T \mathbf{D}\, \mathbf{Q}. \tag{1}$$

The Hencky strain tensor, $\boldsymbol{\varepsilon}$, is defined in Eq. (2):

$$\boldsymbol{\varepsilon} = \mathbf{Q}^T \ln \mathbf{D}\, \mathbf{Q}. \tag{2}$$

An optical or electron micrograph allows for a 2-D strain inversion. The strain tensor, $\boldsymbol{\varepsilon}$, is a 2 by 2 tensor with three independent components that can be computed in the sample reference as seen in the insert in Fig. 7, one along the 1 axis, a second along the 2 axis, and a third shear component. In Fig. 7, the three components for an area of Carrara marble deformed to 11 % compressive strain at $T = 600\,^{\circ}\mathrm{C}$, $P_c = 300\,\mathrm{MPa}$, and a strain rate of $3 \times 10^{-5}\,\mathrm{s}^{-1}$ are contoured over a map of the grain boundaries of the analyzed area. The geological convention is used in which positive strains correspond to shortening strains and negative strains correspond to lengthening strains. Topographic information would be required to compute the full 3-D strain tensor. However, in the split-cylinder setup, the out-of plane component of the strain tensor can be inferred from the 2-D tensor if the deformation is isochoric and axisymmetric as explained in Quintanilla-Terminel and Evans (2016).

3.3 Resolution of the technique

The resolution of the strain analysis technique depends on two main factors that should be assessed for each application before interpreting the strain results. The main sources of error are related to the location of the markers and the strain induced by the sample preparation. Any error in the marker locations will propagate into the strain calculation. This error is a function of the resolution of the images and the image analysis technique used to locate the markers. The second source of error comes from actual local strains produced by

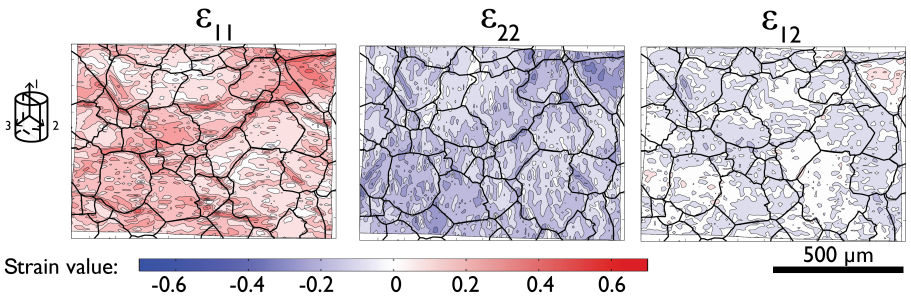

Figure 7. Strain maps for the three components of the 2-D strain tensor for a sample of Carrara marble deformed at $T = 600\,^{\circ}\mathrm{C}$ and $P_c = 300\,\mathrm{MPa}$ to 11 % shortening strain at $3 \times 10^{-5}\,\mathrm{s}^{-1}$. The strain tensor was computed using the n-point technique with $n = 9$. The grain boundaries are overlaid on the strain maps. Positive strains correspond to shortening.

the preparation of the sample. This error has to be estimated with a "zero strain" experiment by measuring the local strain in a sample left under the pressure and temperature conditions for a time length typical of the experiment.

The n-point inversion technique assumes homogeneous deformation for all n points, and it therefore introduces a characteristic spatial dimension for the local inelastic strain. In practice, the inversion is realized point by point; for each point, its $n-1$ neighbors are located. Thus, when n is larger, the computation error is reduced, providing that strain is actually homogenous within the ROI. However, when n is larger, the characteristic length scale of the strain heterogeneity is also larger. Thus, a compromise exists between the resolution of spatial variations in local strain and the errors involved in its calculation (Quintanilla-Terminel and Evans, 2016; Xu and Evans, 2010; Bourcier et al., 2013).

Figure 6 illustrates the different n configurations and their corresponding strain map and strain distribution along the 1 axis (in the sample reference) for a "zero strain" experiment. This experiment was performed on a half cylinder of Carrara marble at $T = 700\,^{\circ}\mathrm{C}$ and $P_c = 300\,\mathrm{MPa}$ in order to evaluate the resolution of the experimental series in Quintanilla-Terminel and Evans (2016). The mean strain is zero for all n point configurations, but the standard deviation is larger for smaller n. Both the "real" strain coming from experimental artifacts and the computational error coming from the marker locations are evaluated. In the Carrara marble series we chose the $9n$ point as a compromise, with a strain gauge length of 20 µm and an experimentally estimated uncertainty in the strain of ± 0.001 (Quintanilla-Terminel and Evans, 2016).

4 Application to creep of rock

The choice of grid design and patterning technique should reflect the test geometry, physical characteristics of the target rocks, and research goals, including specific hypotheses regarding constitutive behavior. The design choices made for tests on Carrara marble and San Carlos olivine, synthetic forsterite, and Solnhofen limestone can be used for illustration. In the first case, Carrara marble deformation by power-law creep (Renner and Evans, 2002; Renner et al., 2002), we wished to investigate the partitioning of the strain between different deformation mechanisms to determine which were dominant and to identify the internal state variables needed for a more accurate flow law (Evans, 2005). Patterns in this study were made using photolithography. In the second case, we wished to observe microstructures produced during dislocation creep in San Carlos olivine (Hansen et al., 2011; Hirth and Kohlstedt, 2003) and during diffusion creep in synthetic forsterite (Dillman, 2016) and Solnhofen limestone (Schmid et al., 1977). Here, our goals included determining the strain contribution of grain boundary sliding in different creep regimes and testing current constitutive models. For this work, we produced patterns with e-beam lithography.

4.1 Grid design and sample geometry

The average grain size of our Carrara marble samples was 130 µm (Xu and Evans, 2010; Quintanilla-Terminel and Evans, 2016); therefore, patterns with micrometer resolution, as formed by photolithography, were optimal. Our designs included circular markers 2 µm in diameter with centers spaced at 10 µm intervals, complemented by a printed numbering system. Thus, even though there were about 1.5 million markers, each could be assigned a unique address. Strain was mapped at a scale of 20 µm across the sample. For MSSM in samples of San Carlos olivine, synthetic forsterite, and Solnhofen limestone, all of which have grain sizes ≤ 10 µm, higher-resolution patterns were necessary. We therefore used electron-beam lithography to print two intersecting grid patterns. In the first, the lines were 500 nm thick and spaced by 4.5 µm; in the second, they were 200 nm thick and spaced by 2 µm. We chose lines rather than circular markers to emphasize localized offsets at grain boundaries.

Photolithography is a flexible technique that can be used to mark surfaces with varying geometry, including split cylinders or cylindrical surfaces (Figs. 2a, b, 8a). E-beam lithography has better spatial resolution but limits the surface geometry. As seen in Sect. 2, the sample has to be flat and not more than 1 mm thick. Two different composite cylinder

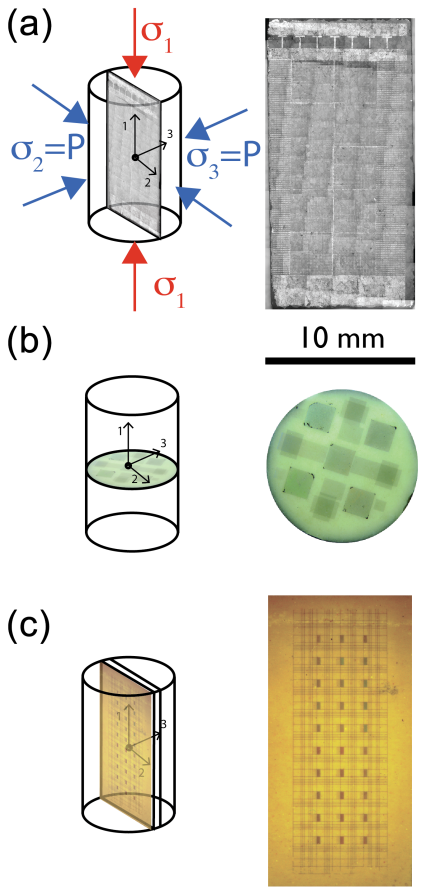

Figure 8. Experimental setup for studying creep in Carrara marble, San Carlos olivine, and fine-grained Solnhofen limestone at high temperatures and $P_c = 300$ MPa in a Paterson Instruments gas apparatus. **(a)** The composite half cylinder is composed of two pieces; one is gridded using photolithography, and the other is polished and sputtered with a window-shaped metal layer. Panels **(b)** and **(c)** show the composite setups used when the patterning involved e-beam lithography. San Carlos olivine was deformed using the setup in panel **(b)**: a patterned 1 mm thick disk was introduced between two short olivine samples. Solnhofen limestone was deformed using the setup in panel **(c)**: a patterned 1 mm thick rectangular slab was introduced between two half cylinders.

sample configurations were used to introduce a 1 mm thick patterned sample. In the first, a 1 mm thick disk of San Carlos olivine disk was placed between two short olivine cylinders (Fig. 8b). In the second, a 1 mm thick rectangular slab of patterned Solnhofen limestone was inserted between two half cylinders (Fig. 8c).

4.2 Application of photolithography: creep of Carrara marble

We used a split-cylinder setup following Raleigh (1965) and Spiers (1979). Half cylinders of "Lorano Bianco" Carrara marble, a standard material for deformation experiments (Molli and Heilbronner, 1999; Heege et. al., 2002), were polished down to a 0.5 µm grit size using aluminum oxide and patterned by photolithography. Optical micrographs of the surfaces were made before and after deformation. Matlab™ was used for the strain computation. The circular markers were identified using a Hough transform and registered with the embedded coordinate system. The 2-D strain tensor was computed using the n-point algorithm. The MSSM technique allowed for an inversion of strain at different scales up to shortening strains of 36 % at a temperature of 700 °C. Notice that strains measured over an ROI at sample scales, macroscales, and microscales have the same average values but larger standard deviations as the spatial scale of measurement decreases (Fig. 9). The markers belonging to each grain are identified and classified; maps of the different strain tensor components can be used to determine strain accommodation owing to slip along grain boundaries, twinning, and intragranular deformation (Quintanilla-Terminel, 2014). Figure 10 shows samples shortened to 11 % at $T = 400$, 500, 600, and 700 °C and $P_c = 300$ MPa; Fig. 11 illustrates samples shortened to 11, 22, and 36 % at 600 °C. In all experiments, the means of the local strains agreed remarkably well with those measured during the mechanical tests. Importantly, the spatial heterogeneity varied with strain and temperature. For more detail, see Quintanilla-Terminel and Evans (2016).

4.3 Application of electron-beam lithography: creep of San Carlos olivine and synthetic forsterite

The greatest challenge in studying strain distributions during creep in olivine rocks is the separation of the surfaces after deformation. Because creep tests must be carried out at $T > 1000$ °C and $P_c = 300$ MPa, the metal of the grid and the rock surface strongly adhere. Nonetheless, the results described here are promising and suggest that, with further work, strain distributions during grain boundary sliding might be successfully measured (Figs. 12–13).

4.3.1 Compression experiments on San Carlos olivine at 300 MPa and 1150 °C

We used electron-beam lithography to pattern monophase polycrystalline samples prepared from powders of San Carlos olivine, Fo_{90}. First, samples were fabricated by cold pressing powders into a nickel can, followed by hot-pressing at $P_c = 300$ MPa and $T = 1250$ °C for 3 h (Hansen et al., 2011). A 1 mm thick slice was cut from the hot-pressed cylinder and one side was ground and polished in a final step using lapping films with 0.5 µm diamond grit. The olivine wafers were then patterned following the protocol described in Sect. 2. The rest of the cylinder was cut in half, one was end polished, and the three pieces were assembled as shown in Fig. 8b. This composite sample was deformed at $P_c = 300$ MPa, $T = 1150$ °C, and a constant strain rate of

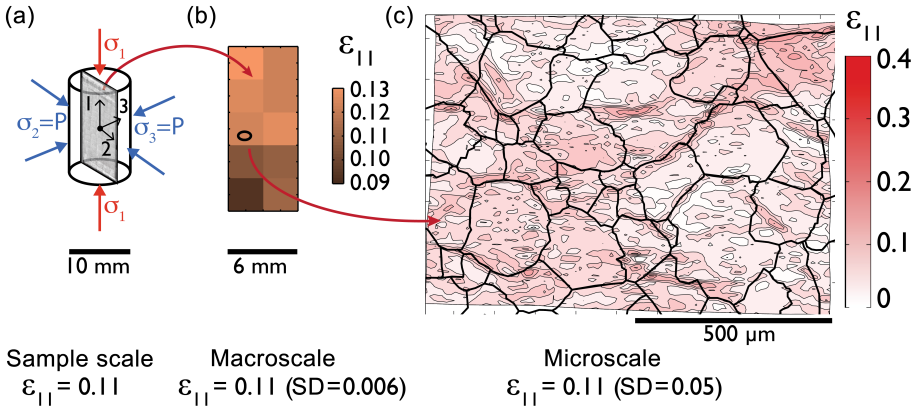

Figure 9. Strain maps over different regions of interest for a Carrara marble split cylinder deformed at $T = 600\,^{\circ}\mathrm{C}$ and $P_c = 300\,\mathrm{MPa}$ to 11 % shortening strain at $3 \times 10^{-5}\,\mathrm{s}^{-1}$ **(a)**. The component along the shortening direction of the strain tensor, ε_{11}, was computed at different scales. In panel **(b)**, ε_{11} was computed over the whole sample with a gauge length of 3 mm (macroscale). In panel **(c)**, ε_{11} was computed over a smaller region of interest with a 20 µm gauge length (microscale) and is mapped with the overlaying grain boundaries. Positive strains correspond to shortening. Modified after Quintanilla-Terminel and Evans (2016).

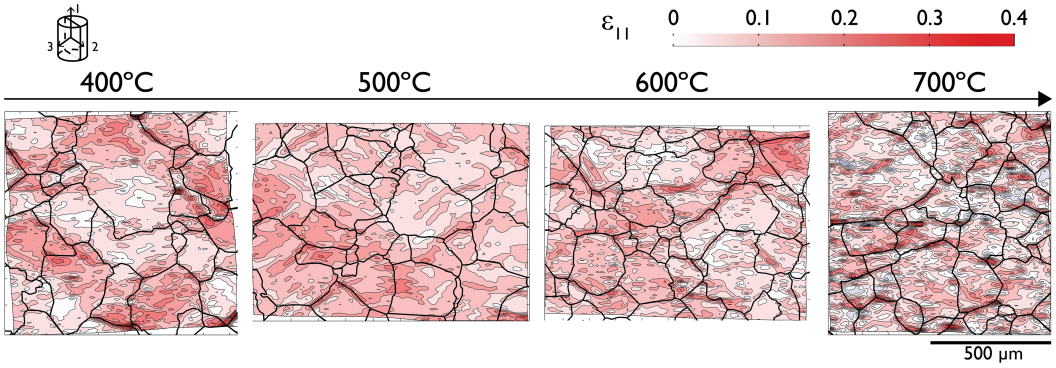

Figure 10. Strain maps for ε_{11} computed with an n-point technique (with $n = 9$) for samples of Carrara marble deformed at $T = 400$, 500, 600, and 700 °C, $P_c = 300\,\mathrm{MPa}$, and $3 \times 10^{-5}\,\mathrm{s}^{-1}$ to 11 % shortening strain. The strain component along the shortening direction is mapped with the overlaying grain boundaries. Shortening is positive. Note the concentration of strain along grain boundaries and intragranular features as T increases.

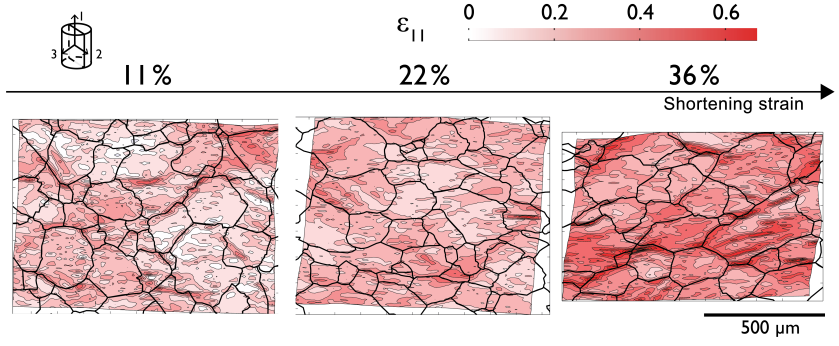

Figure 11. Strain maps for ε_{11} computed with an n-point technique (with $n = 9$) for samples of Carrara marble deformed at $T = 600\,^{\circ}\mathrm{C}$, $P_c = 300\,\mathrm{MPa}$, and $3 \times 10^{-5}\,\mathrm{s}^{-1}$ to 11, 22, and 36 % shortening strain. The strain component along the shortening direction is mapped with the overlaying grain boundaries. Positive strains correspond to shortening strains.

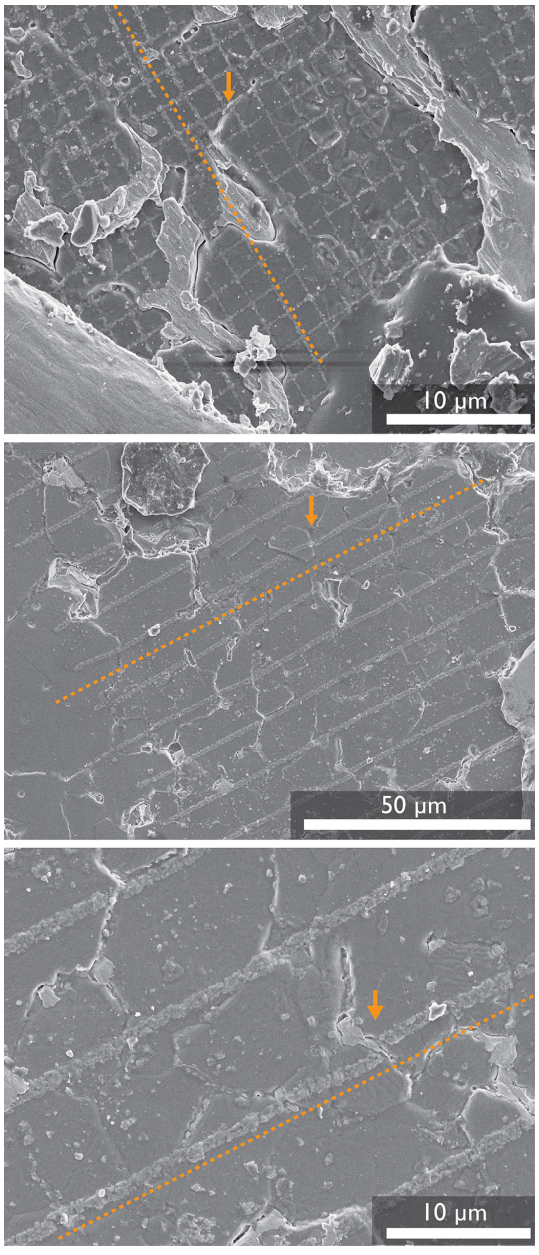

Figure 12. Secondary electron images of a gridded fine-grained San Carlos olivine after deformation at $T = 1100\,°C$ and $P_c = 300\,MPa$ to 5 % shortening at $1 \times 10^{-5}\,s^{-1}$. The deformed lines show clear offsets at grain boundaries. The dotted orange lines show evidence of the deformation of the lines in the grid. The orange arrows show grain boundary displacement.

$1 \times 10^{-5}\,s^{-1}$ to 15 % shortening strain in a gas-medium high-pressure apparatus (Hansen et al., 2011). The strength at a steady state of the composite, 245 MPa, is in excellent agreement with that determined from earlier tests with intact cylinders (Hansen et al., 2011).

Recovering the grid after deformation was more challenging because of the high temperatures and normal loads on the marked surface. We experimented with different metals and separation techniques. Sputtering a window shape with a high-melting-temperature metal, such as tungsten, on the facing sample (a technique similar to the one used for Carrara marble) was unsuccessful, and the two faces still could not be separated. Inserting a thin (0.01 mm), ring-shaped, nickel foil between the gridded surface and the facing surface was still not sufficient, but the gridded surface was successfully recovered if a full nickel foil was placed between both surfaces. Secondary electron micrographs of grids with lines 200 nm and 1 µm thick show offsets of 0.5 to 1 µm along the grain boundaries (Fig. 12a, b). On a recovered area (Fig. 13a), the strain was inverted using the n-point algorithm described above; the component ε_{22} is mapped in Fig. 13b. Note that the gridded surface is perpendicular to the shortening axis compared to the Carrara marble tests in which the gridded surface was parallel to the shortening axis (Figs. 10–11). Because the size of the recovered area is small, we cannot draw meaningful conclusions regarding the partitioning between intragranular strain and grain boundary sliding, but the technique offers further opportunities for success.

4.3.2 Compression experiments on forsterite at 1 atm and 1100 °C

Samples of synthetic forsterite were synthesized following Koizumi et al. (2010). After gridding, they were deformed at $T = 1250\,°C$ and $P_c = 1\,atm$ (Dillman, 2016) with the grid on an outer surface of a sample with a square cross section. The tests used a grid 500 nm thick and were designed to be compared with previous measurements of creep (Dillman, 2016) using a line offset caused by grain boundary sliding (Langdon, 2006). Grid recovery for these samples was much easier because deformation occurred under atmospheric pressure. We used an AFM to measure the vertical displacement of grains and to map the deformed grid (Fig. 14). The state of the initially regular grid after deformation highlights the deformation occurring along grain boundaries. 2-D offsets of $\sim 500\,nm$ are evident. More details on the 1 atm compression experiments on synthetic forsterite can be found in Dillman (2016).

4.3.3 Creep of fine-grained Solnhofen limestone

Three-piece samples of Solnhofen limestone were prepared (Fig. 8c), gridded using e-beam lithography, and deformed in compression in gas-medium apparatus (Paterson, 1990) at $T = 700\,°C$ and $P_c = 300\,MPa$ to a shortening strain of 9 % at a strain rate of $3 \times 10^{-4}\,s^{-1}$. The patterned surfaces could be separated without the addition of a metal foil, and the deformed pattern was easily found using electron microscopy. In Fig. 15 with the two secondary electron micrographs of the same area before and after deformation, the grid and the deformed lines are clearly visible; however, the grain structure is not. Additional characterization permitting the identi-

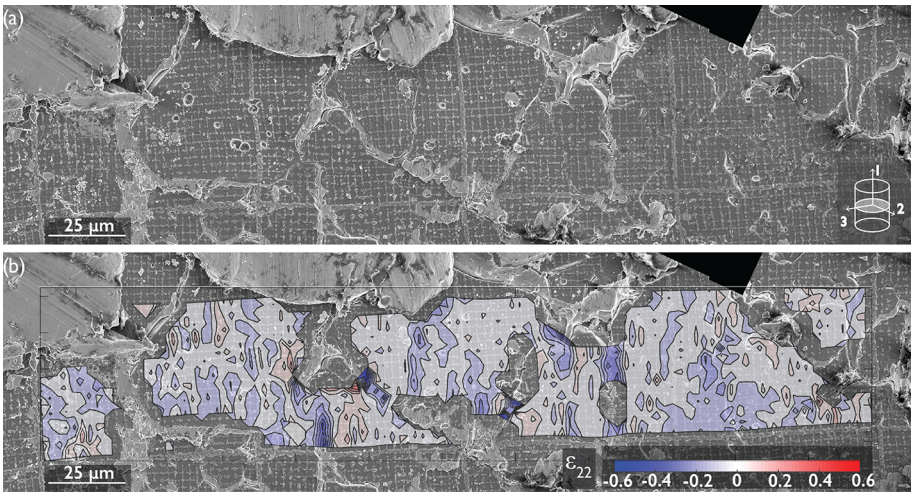

Figure 13. Strain inversion on a recovered grid in a fine-grained sample of San Carlos olivine deformed at $T = 1100\,^{\circ}\mathrm{C}$ and $P_c = 300\,\mathrm{MPa}$ to 5 % deformation at $1 \times 10^{-5}\,\mathrm{s}^{-1}$. **(a)** Secondary electron image of the recovered area and **(b)** a superposed strain map of ε_{22}, a component of the strain tensor that is perpendicular to the shortening direction.

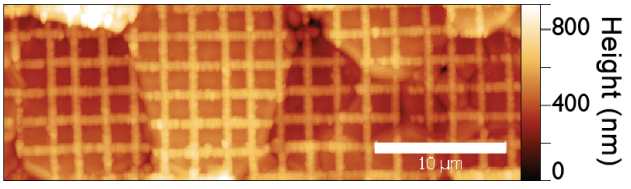

Figure 14. Atomic force micrograph of a deformed grid in synthetic forsterite deformed at $T = 1110\,^{\circ}\mathrm{C}$ and $P_c = 1$ atm to 5 % shortening. The chromium lines are about 110 nm thick and are clearly visible in the height map. The grain structure is also clearly visible and both the height difference and the offset of the lines show evidence of grain displacement. Amanda Dillman performed the deformation experiment and the AFM observations for this sample.

fication of the grain boundaries (possibly imaging with electron backscatter diffraction) will be necessary to evaluate the contribution of the grain boundary sliding to the total strain. Nonetheless, this application demonstrates that the deformation of the lines and grid is visible and that the electron-beam lithography provides the required resolution to quantify the strain at the granular level.

5 Conclusions

Patterning using photolithography and e-beam lithography can provide maps of strain calculated over spatial scales of 10–0.5 µm. The experimental preparation is technologically demanding and labor intensive, but MSSM is a unique characterization tool that yields a detailed description of strain accommodation within intragranular and intergranular regions. The experimental protocols described here can be adapted to many other rocks, and the pattern can be designed for

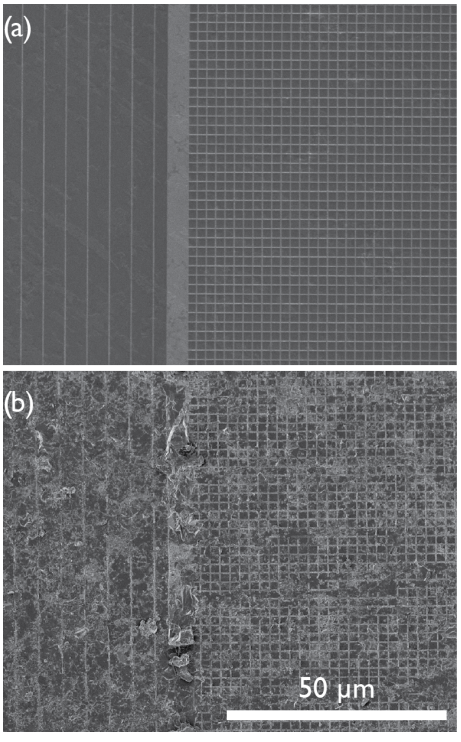

Figure 15. Secondary electron micrographs of a patterned Solnhofen limestone sample **(a)** before deformation and **(b)** after deformation at $T = 700\,^{\circ}\mathrm{C}$ and $P_c = 300\,\mathrm{MPa}$ to 9 % shortening strain at $3 \times 10^{-4}\,\mathrm{s}^{-1}$. Before deformation, the pattern consisted of 200 nm wide lines spaced every 5 µm and a grid of 200 nm lines spaced every 2 µm. The lines were made of 110 nm thick chromium. After deformation, the lines are clearly deformed but the grain structure is not apparent.

specific purposes. The MSSM technique has the potential to improve the interpretation of microstructural observations of rocks deformed in nature and in the lab, constrain the partitioning of strain among several deformation mechanisms, and improve the constitutive modeling of creep mechanisms in the Earth.

Data availability. All figures and underlying research data used in this paper can be accessed at https://doi.org/10.5281/zenodo.822490 (Quintanilla-Terminel et al., 2017) (figures and data related to creep of olivine) and https://doi.org/10.5281/zenodo.822501 (Quintanilla-Terminel and Evans, 2017) (data related to the Carrara marble deformation series).

Competing interests. The authors declare that they have no conflict of interest.

Special issue statement. This article is part of the special issue "Analysis of deformation microstructures and mechanisms on all scales". It is a result of the EGU General Assembly 2016, Vienna, Austria, 17–22 April 2016.

Acknowledgements. Matej Pec is acknowledged for his help in acquiring the SEM pictures. Amanda Dillman is acknowledged for providing the data related to the forsterite sample and for her help in acquiring the AFM data. The lithography techniques were developed at the Minnesota Nano Center (MNC) of the University of Minnesota and at the MIT Micro Technology Laboratories (MTL). AQT thanks Bryan Cord at the MNC and Kurt Broderick at the MTL for their guidance through the fabrication processes. We benefitted from enriching discussions with Matej Pec, Amanda Dillman, Renée Heilbronner, Holger Stünitz, and William Durham and thoughtful reviews by Lars Hansen and an anonymous reviewer. Support through NSF grants EAR-1520647 (UMN) and 145122 (MIT) is gratefully acknowledged.

Edited by: Florian Fusseis
Reviewed by: Lars Hansen and one anonymous referee

References

Allais, L., Bornert, M., Bretheau, T., and Caldemaison, D.: Experimental characterization of the local strain field in a heterogeneous elastoplastic material, Acta Metallurgica et Materialia, 42, 3865–3880, https://doi.org/10.1016/0956-7151(94)90452-9, 1994.

Ashby, M. F.: A First Report on Deformation-Mechanism Maps, Acta Metallurgica, 20, 887–897, https://doi.org/10.1016/0001-6160(72)90082-X, 1972.

Biery, N., De Graef, M., and Pollock, T. M.: A Method for Measuring Microstructural-Scale Strains Using a Scanning Electron Microscope: Applications to γ-Titanium Aluminides, Metall. Mater. Trans. A, 34, 2301–2313, 2003.

Bornert, M., Brémand, F., Doumalin, P., Dupré, J.-C., Fazzini, M., Grédiac, M., Hild, F., Mistou, S., Molimard, J., Orteu, J.-J., Robert, L., Surrel, Y., Vacher, P., and Wattrisse, B.: Assessment of Digital Image Correlation Measurement Errors: Methodology and Results, Exp. Mech., 49, 353–370, https://doi.org/10.1007/s11340-008-9204-7, 2008.

Bourcier, M., Bornert, M., Dimanov, A., Héripré, E., and Raphanel, J. L.: Multiscale Experimental Investigation of Crystal Plasticity and Grain Boundary Sliding in Synthetic Halite Using Digital Image Correlation, J. Geophys. Res.-Solid Earth, 118, 511–526, 2013.

Bruck, H. A., McNeill, S. R., Sutton, M. A., and Peters, W. H.: Digital Image Correlation Using Newton-Raphson Method of Partial Differential Correction, Exp. Mech., 29, 261–267, https://doi.org/10.1007/BF02321405, 1987.

Chauve, T., Montagnat, M., and Vacher, P.: Strain Field Evolution during Dynamic Recrystallization Nucleation; A Case Study on Ice, Acta Materialia, 101, 116–124, 2015.

Dautriat, J., Bornert, M., Gland, N., Dimanov, A., and Raphanel, J.: Localized Deformation Induced by Heterogeneities in Porous Carbonate Analysed by Multi-Scale Digital Image Correlation, Tectonophysics, 503, 100–116, 2011.

Dillman, A.: Influence of Grain Boundaries and Their Composition on the Deformation Strength of High-Purity, Synthetic Forsterite, available at: http://conservancy.umn.edu/handle/11299/182257 (last access: July 2017), 2016.

Dong, J., Liu, J., Kang, G., Xie, J., and Wang, Y.: Pushing the Resolution of Photolithography down to 15 nm by Surface Plasmon Interference, Scientific Reports, 4, 5618, https://doi.org/10.1038/srep05618, 2014.

Evans, B.: Creep constitutive laws for rocks with evolving structure, in: High-Strain Zones: Structure and Physical Properties, edited by: Bruhn, D. and Burlini, L., 329–346, Geological Society of London, London, UK, https://doi.org/10.1144/GSL.SP.2005.245.01.16, 2005.

Frost, H. J. and Ashby, M. F.: Deformation-Mechanism Maps: The Plasticity and Creep of Metals and Ceramics, Pergamon Press, 1982.

Ghadbeigi, H., Pinna, C., and Celotto, S.: Quantitative strain analysis of the large deformation at the scale of microstructure: Comparison between digital image correlation and microgrid techniques, Exp. Mech., 52, 1483–1492, https://doi.org/10.1007/s11340-012-9612-6, 2012.

Grennerat, F., Montagnat, M., Castelnau, O., Vacher, P., Moulinec, H., Suquet, P., and Duval, P.: Experimental Characterization of the Intragranular Strain Field in Columnar Ice during Transient Creep, Acta Materialia, 60, 3655–3666, https://doi.org/10.1016/j.actamat.2012.03.025, 2012.

Hansen, L. N., Zimmerman, M. E., and Kohlstedt, D. L.: Grain Boundary Sliding in San Carlos Olivine: Flow Law Parameters and Crystallographic-Preferred Orientation, J. Geophys. Res.-Solid Earth (1978–2012), 116, B08201, https://doi.org/10.1029/2011JB008220, 2011.

Hiraga, T.: Grain rotation during diffusion creep of forsterite + diopside, Abstract T51I-03 presented at 2015 Fall Meeting, AGU, San Francisco, Calif., 14–18 December, 2015.

Hirth, G. and Kohlstedt, D.: Rheology of the Upper Mantle and the Mantle Wedge: A View from the Experimentalists, Inside the Subduction Factory, 138, 83–105, 2003.

Karimi, R.: Plastic flow study using the microgrid technique, Mater. Sci. Eng., 63, 267–276, https://doi.org/0025-5416/84, 1984.

Koizumi, S., Hiraga, T., Tachibana, C., Tasaka, M., Miyazaki, T., Kobayashi, T., Takamasa, A., Ohashi, N., and Sano, S.: Synthesis of Highly Dense and Fine-Grained Aggregates of Mantle Composites by Vacuum Sintering of Nano-Sized Mineral Powders, Phys. Chem. Miner., 37, 505–518, https://doi.org/10.1007/s00269-009-0350-y, 2010.

Langdon, T. G.: Grain Boundary Sliding Revisited: Developments in Sliding over Four Decades, J. Mater. Sci., 41, 597–609, https://doi.org/10.1007/s10853-006-6476-0, 2006.

Mack, C. A.: Field Guide to Optical Lithography, Spi edition. Bellingham, Wash: SPIE Publications, 2006.

Malvern, L. E.: Introduction to the Mechanics of a Continuous Medium, Prentice-Hall, 154–183, 1969.

Manfrinato, V. R., Zhang, L., Su, D., Duan, H., Hobbs, R. G., Stach, E. A., and Berggren, K. K.: Resolution Limits of Electron-Beam Lithography toward the Atomic Scale, Nano Letters, 13, 1555–1558, https://doi.org/10.1021/nl304715p, 2013.

Martin, G., Sinclair, C. W., and Lebensohn, R. A.: Microscale Plastic Strain Heterogeneity in Slip Dominated Deformation of Magnesium Alloy Containing Rare Earth, Mater. Sci. Eng.: A, 603, 37–51, https://doi.org/10.1016/j.msea.2014.01.102, 2014.

Molli, G. and Heilbronner, R.: Microstructures Associated with Static and Dynamic Recrystallization of Carrara Marble (Alpi Apuane, NW Tuscany, Italy), Geologie En Mijnbouw, 78, 119–126, https://doi.org/10.1023/A:1003826904858, 1999.

Moulart, R., Rotinat, R., Pierron, F., and Lerondel, G.: On the realization of microscopic grids for local strain measurement by direct interferometric photolithography, Opt. Laser. Eng., 45, 1131–1147, https://doi.org/10.1016/j.optlaseng.2007.06.009, 2007.

Paterson, M. S.: Rock deformation experimentation, in Brittle-Ductile Transition in: Rocks, Heard Volume, edited by: Duba, A. G., Durham, W. B., Handin, J. W., and Wang, H. F., 187–194, Am. Geophys. Union, Washington, 1990.

Quintanilla-Terminel, A.: Strain Heterogeneity during Creep of Carrara Marble, Thesis, Massachusetts Institute of Technology, available at: http://dspace.mit.edu/handle/1721.1/95556 (last access: July 2017), 2014.

Quintanilla-Terminel, A. and Evans, B.: Heterogeneity of Inelastic Strain during Creep of Carrara Marble: Microscale Strain Measurement Technique, J. Geophys. Res.-Solid Earth, 121, 2016JB012970, https://doi.org/10.1002/2016JB012970, 2016.

Quintanilla-Terminel, A. and Evans, B.: Data set of microscale strain for creep of Carrara marble [Data set], Zenodo, available at: https://doi.org/10.5281/zenodo.822501 (last access: July 2017), 2017.

Quintanilla-Terminel, A., Zimmerman, M. E., Evans, B., and Kohsltedt, D. L.: Data set for Microscale and nanoscale strain mapping techniques applied to creep of rocks [Data set], Zenodo, available at: https://doi.org/10.5281/zenodo.822490 (last access: 7 July 2017), 2017.

Raleigh, C. B.: Glide Mechanisms in Experimentally Deformed Minerals, Science, 150, 739–741, https://doi.org/10.1126/science.150.3697.739, 1965.

Razegui, M.: Fundamentals of Solid State Engineering, Springer US, 615–664, 2006.

Reddy, J. N.: An Introduction to Continuum Mechanics, Cambridge University Press, 68–84, 2013.

Renner, J. and Evans, B.: Do Calcite Rocks Obey the Power-Law Creep Equation?, Geological Society, London, Special Publications, 200, 293–307, https://doi.org/10.1144/GSL.SP.2001.200.01.17, 2002.

Renner, J., Evans, B., and Siddiqi, G.: Dislocation Creep of Calcite, J. Geophys. Res., 107, 2364, https://doi.org/10.1029/2001JB001680, 2002.

Schmid, S. M., Boland, J. N., and Paterson, M. S.: Superplastic Flow in Finegrained Limestone, Tectonophysics, 43, 257–291, https://doi.org/10.1016/0040-1951(77)90120-2, 1977.

Sharpe, W. N.: Springer handbook of experimental solid mechanics, Springer, Berlin, 2008.

Spiers, C.: Fabric Development in Calcite Polycrystals Deformed at 400 °C, Bull. Mineral., 102, 282–289, 1979.

Sutton, M. A., Orteu, J. J., and Schreier, H.: Image Correlation for Shape, Motion and Deformation Measurements: Basic Concepts,Theory and Applications, 2009 edition, New York, N.Y: Springer, 2009.

Ter Heege, J. H., De Bresser, J. H. P., and Spiers, C. J.: The Influence of Dynamic Recrystallization on the Grain Size Distribution and Rheological Behaviour of Carrara Marble Deformed in Axial Compression, Geological Society, London, Special Publications, 200, 331–553, https://doi.org/10.1144/GSL.SP.2001.200.01.19, 2002.

Vieu, C., Carcenac, F., Pepin, A., Chen, Y., Mejias, M., Lebib, A., Manin-Ferlazzo, L., Couraud, L., and Launois, H.: Electron Beam Lithography: Resolution Limits and Applications, Appl. Surf. Sci., 164, 111–117, 2000.

Wu, A., de Graef, M., and Pollock, T. M.: Grain-scale strain mapping for analysis of slip activity in polycrystalline b2rual, Philosophical Magazine, 86, 3995–4008, 2006.

Xu, L. and Evans, B.: Strain Heterogeneity in Deformed Carrara Marble Using a Microscale Strain Mapping Technique, J. Geophys. Res.-Solid Earth, 115, B04202, https://doi.org/10.1029/2009JB006458, 2010.

Yasin, S., Hasko, D. G., and Ahmed, H.: Comparison of MIBK/IPA and Water/IPA as PMMA Developers for Electron Beam Nanolithography, Microelectronic Engineering, Micro- and Nano-Engineering, 2001, 61–62 (July), 745–753, https://doi.org/10.1016/S0167-9317(02)00468-9, 2002.